Vol. 32 • No. 10 • March 2 • 2022

www.afm-journal.de

ADVANCED FUNCTIONAL MATERIALS

WILEY-VCH

ADVANCED FUNCTIONAL MATERIALS
www.afm-journal.de

Triculture Model of In Vitro BBB and its Application to Study BBB-Associated Chemosensitivity and Drug Delivery in Glioblastoma

Suyeong Seo, Seung-Yeol Nah, Kangwon Lee, Nakwon Choi,* and Hong Nam Kim**

Physiologically, brain tumors interact with surrounding vascular and glial cells, and change their responses to survive in brain tissue-specific microenvironments. A major difficulty in brain tumor treatment is caused by the organism's high resistance to pharmaceutical drugs and poor blood–brain barrier (BBB) penetration. Therefore, mimicking the physiological environment of brain tumors on in vitro platforms can aid in predicting the cellular response to drugs. Here, an engineered 3D human glioblastoma in vitro platform that is integrated with a tricultured BBB is presented. First, the barrier function of the constructed BBB model and its reversibility are characterized, after administrating BBB-opening agents through the microvasculature. The brain tumor cells that are cocultured in the BBB show a more aggressive growth pattern and high drug resistance, as well as secreting high concentrations of inflammatory cytokines. Finally, the delivery of BBB-nonpenetrating drugs are promoted by chemically opening the BBB. The results of this study indicate that the platform can potentially study the physiology of the BBB, and monitor drug responses based on the interaction of the brain tumor and BBB.

1. Introduction

Tumors dynamically interact with the surrounding environment, and can rapidly alter and adapt their metabolism with the microenvironment, leading to the development of resistance to any therapeutic agents that limits several treatment strategies.[1,2] The tumor microenvironment (TME), comprising cellular (i.e., nontumorous cells interacting with cancer cells, such as stromal and immune cells) and noncellular components (i.e., extracellular matrix, vasculature, and cytokines), is a critical regulator of the progression and evolution of malignancies as well as the distant metastasis of tumor.[3–6] Furthermore, it is involved in the acquired resistance of tumors to therapeutic drugs by altering relevant signaling pathways, resulting in reduced drug delivery efficiency and efficacy. Therefore, recent studies have focused on accurately replicating organ-specific TME, using engineered platforms, to address the complexity of the TME that significantly affects tumor behavior, drug responses, and patient outcomes.[7–10]

Several in vitro tumor models, which used human umbilical vein endothelial cells (HUVECs), human lung fibroblasts (HLFs), and cancer cell lines in fibrin-based hydrogels to promote vascularization around tumor spheroids, were developed to mimic the TME, and focused on the interaction between the tumor and vasculature.[11–14] However, the drawbacks of these models include the difficulty of observing tumor-associated changes in the

S. Seo, N. Choi, H. N. Kim
Brain Science Institute
Korea Institute of Science and Technology (KIST)
Seoul 02792, Republic of Korea
E-mail: nakwon.choi@kist.re.kr; hongnam.kim@kist.re.kr

S. Seo
Program in Nano Science and Technology
Graduate School of Convergence Science and Technology
Seoul National University
Seoul 08826, Republic of Korea

The ORCID identification number(s) for the author(s) of this article can be found under https://doi.org/10.1002/adfm.202106860.

DOI: 10.1002/adfm.202106860

S.-Y. Nah
Department of Physiology
College of Veterinary Medicine
Konkuk University
Seoul 05029, Republic of Korea

K. Lee
Department of Applied Bioengineering
Graduate School of Convergence Science and Technology
Seoul National University
Seoul 08826, Republic of Korea
E-mail: kangwonlee@snu.ac.kr

N. Choi, H. N. Kim
Division of Bio-Medical Science & Technology
KIST School
Korea University of Science and Technology (UST)
Seoul 02792, Republic of Korea

N. Choi
KU-KIST Graduate School of Converging Science and Technology
Korea University
Seoul 02841, Republic of Korea

structure and function of normal blood vessels (as tumor cells influence blood vessel formation at an early stage) and the difficulty in controlling the vascular dimension and structure and isolating the tumor cells for further assays.[15,16] Furthermore, utilizing HUVEC and lung fibroblast-based models is not suitable for investigating brain tumor pathophysiology, because tissue-specific tumor cells usually interact with tissue-specific microenvironmental factors.[17,18]

In this study, we aim to replicate the complicated glioblastoma multiforme (GBM) microenvironment and the anatomical features and functionality of the in vivo blood–brain barrier (BBB) (**Figure 1**B), and demonstrate the influence of the GBM microenvironment on tumor behavior and drug delivery. Thus, we fabricated a human BBB model by coculturing BBB-composing cells within a 3D hydrogel matrix. The barrier functions of the constructed BBB were verified by visualizing the expression of BBB-specific markers, and by measuring the vascular permeability. Additionally, we investigated the stimuli-response of the BBB structure, by administering inflammatory cytokines and BBB-opening agents. Then, we extended the

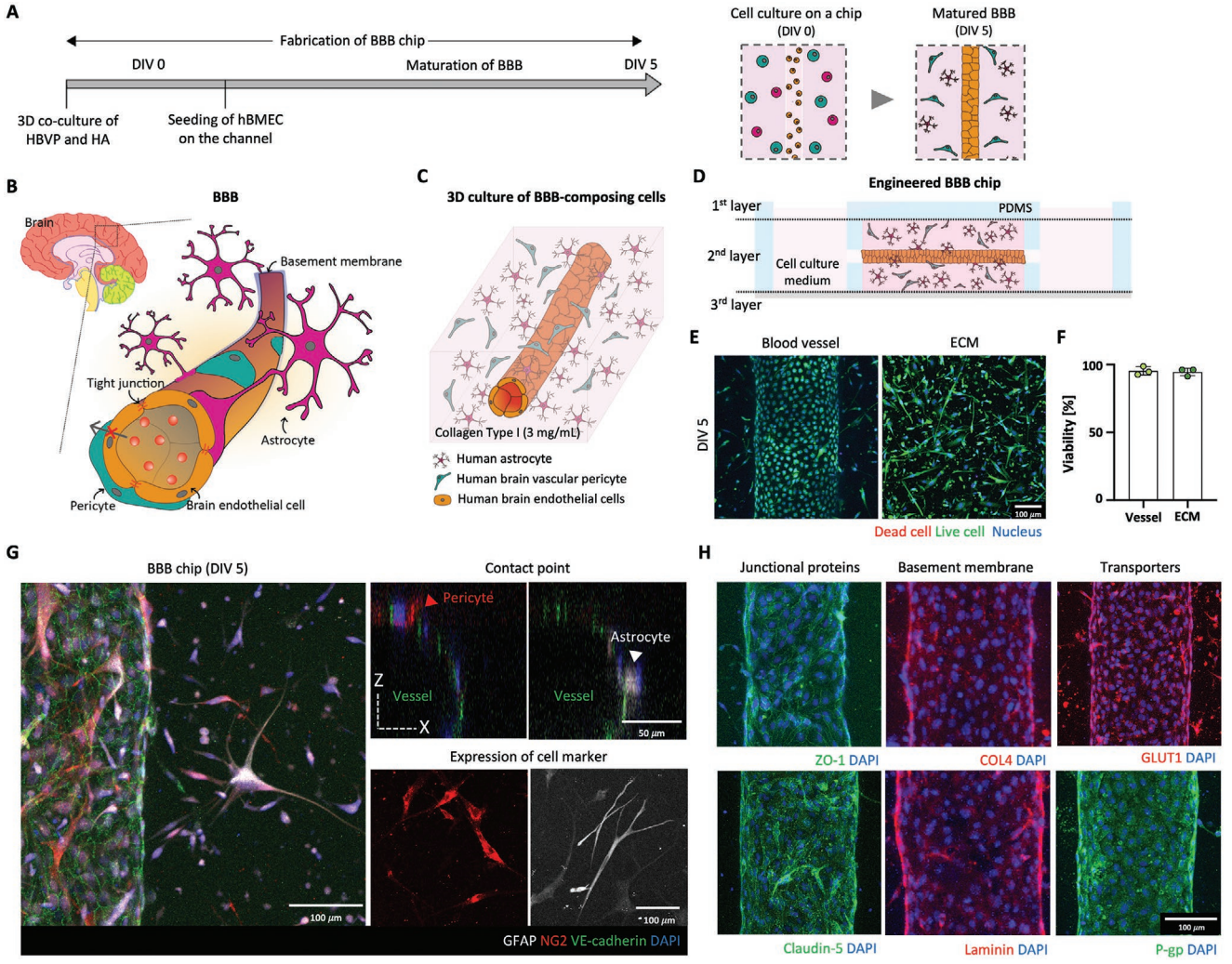

Figure 1. Fabrication of the in vitro human BBB model. A) Timeline of fabricating in vitro human BBB chips. B) Schematic of the BBB. The BBB comprises brain endothelial cells, pericytes, and astrocytes. The endothelial cells organized tight junctions with adjacent endothelial cells, and then, formed a monolayer covered with pericytes and astrocytes. Pericytes shared the basement membrane with the endothelium through direct contact to stabilize the blood vessel. Astrocytic-end feet are also in direct contact with the endothelium, to modulate the BBB in physiological and pathological conditions. C) Schematic of the 3D culture of BBB-composing cells. The endothelium formed along the linear vessel within the collagen embedded with pericytes and astrocytes, displaying similar anatomical structure with in vivo BBB. D) Cross-section of engineered BBB chip. The cell culture medium was supplied to the endothelium by the gravity-driven flow. E) Live cells were stained with calcein-AM (green) and dead cells were stained with PI (red) (scale bar: 100 μm). F) Viability of all cells cultured on the chip on day 5. All cells in the blood vessel and culture within the collagen (ECM) showed viability greater than 90% ($n = 3$ for each condition). G) Confocal image of the engineered BBB chip. Cocultured cells were verified by staining their specific markers (endothelial cells: VE-cadherin, astrocyte: GFAP, pericyte: NG2) on day 5. The endothelial cells organized the vessel closely interacting with the astrocyte and pericyte (scale bar: 100 μm). Representative orthogonal views on the *XZ* plane show contacts by astrocyte and pericyte to the endothelium (scale bar: 50 μm). H) Physical barrier of the blood vessel was confirmed by staining tight junctions (ZO-1 and Claudin-5). The formation of the basement membrane surrounding the blood vessel was also confirmed by staining collagen type IV and laminin. Specific transporters and efflux pump on the endothelial cells were visualized by staining GLUT1 and P-glycoprotein (scale bar: 100 μm).

BBB chip as a human GBM model by incorporating the GBM spheroid in the proximity of the matured BBB, promoting BBB–GBM interaction. We monitored both GBM-induced vascular changes and behavioral and drug response changes of GBM due to cell-to-cell interactions. Finally, we demonstrated the co-administration effect of the BBB-nonpenetrant drug and BBB-opening agents, in an attempt to facilitate the entry of the drug into the neuronal region.

2. Results

2.1. Fabrication of the In Vitro Human BBB Model

The proposed device is composed of three layers: a lid as the top layer; a middle polydimethylsiloxane (PDMS) layer with a 4×10 mm rectangular chamber and three parallel microchannels that supplies medium to cells in the hydrogel matrix; and a sliding glass as the bottom layer (Figure 1D). A mixture of cells, comprising human brain vascular pericyte (HBVP) and human astrocyte (HA), and collagen was injected into the chamber with preinserted microneedles, and incubated for 30 min. Then, after the collagen was completely gelated, the microneedles were removed, and the human brain microvascular endothelial cell (HBMEC) suspension was infused into the channel. The seeded endothelial cells rapidly adhered to the hollow cylindrical channel of the collagen, forming a cylindrical brain endothelium surrounded by pericytes and astrocytes after 5 days of culture (Figure S1, Supporting Information). The chips were maintained under gravity-driven flow providing sufficient supply of nutrient and oxygen through the collagen space with high Péclet number ($>10^3$).

We evaluated the optimal concentration of collagen in the range of 1–5 mg mL^{-1} based on the cell morphology and vascular integrity. The astrocytes cultured in the soft matrix displayed more in vivo-like morphology, indicating radially-arranged foot processes with small cell bodies (Figure S2A, Supporting Information). Additionally, previous studies have shown that glial cells sensitively respond to the density of the surrounding matrix, and can change their morphologies and the expression of inflammatory and gliosis-related genes.[19,20] Moreover, we observed a leakage of 376 Da fluorescein sodium salt from the blood vessel within the selected range of 1–3 mg mL^{-1} collagen concentrations (Figure S2B, Supporting Information). The brain endothelium formed in the stiff environment (3 mg mL^{-1}) has a tighter barrier with low permeability and more stabilized structure than those cultured in a soft matrix ($P_{1\,\mathrm{mg\,mL^{-1}}} = 4.48 \times 10^{-6} \pm 2.08 \times 10^{-6}$ cm s^{-1}; $P_{2\,\mathrm{mg\,mL^{-1}}} = 5.17 \times 10^{-6} \pm 1.97 \times 10^{-6}$ cm s^{-1}; $P_{3\,\mathrm{mg\,mL^{-1}}} = 1.23 \times 10^{-6} \pm 5.01 \times 10^{-7}$ cm s^{-1}) (Figure S2C, Supporting Information). Therefore, we have chosen 3 mg mL^{-1} as the optimal collagen concentration for collagen type I used in the 3D cell culture. Furthermore, we confirmed the viability of the cells cultured in the chips, as shown in Figure 1E, which exhibited an excellent viability at approximately 90% at day 5 (blood vessel: 95.4 ± 3.1%; ECM: 94.6 ± 2.8%) (Figure 1F). The engineered in vitro BBB was visualized after 5 days of vascular maturation by staining all the cells with their specific markers (endothelial cells: vascular endothelial (VE)-cadherin; astrocytes: GFAP; pericyte: NG2) (Figure 1G). We observed pericytes closely distributed around the blood vessels, which organized direct contacts, enhancing the vascular integrity (Figure S3, Supporting Information). Moreover, astrocytes encircle the endothelium by spreading their end feet. Meanwhile, the physical barrier, localized between adjacent endothelial cells, was verified by staining junctional proteins (tight junction: ZO-1 and claudin-5; adherens junction: VE-cadherin). The basement membrane remodeled by endothelial cells was also visualized by staining collagen type 4 and the laminin. Last, the presence of BBB functional transporters was also confirmed through the expression of glucose transporter 1 (GLUT1) and P-glycoprotein (P-gp) (Figure 1I).

2.2. Functional Characterization of the Engineered Human BBB

We measured the transendothelial permeability of fluorescent dyes (molecular weights (MW): 376 Da, 4 kDa, and 40 kDa) across the engineered brain blood vessel, to evaluate the barrier functionality of the BBB structure. The BBB is known to transport molecules in a size-dependent manner. For example, molecules with MW smaller than 500 Da are transported through the paracellular pathway.[16] We evaluated the transendothelial permeability of our engineered BBB by using three fluorescent model molecules with MW of 376 Da, 4 kDa, and 40 kDa. The fluorescent solution was infused into the brain endothelium, and its leakage was monitored by scanning sequential images (**Figure 2**A). Moreover, we confirmed the effect of coculture on vascular permeability, resulting in a decreasing permeability over the culture period (days in vitro 1–5) (Figure 2B). In particular, the barrier function was tighter in the triculture (average $P_{4\mathrm{kDa,\,tri}} = 2.54 \times 10^{-8} \pm 2.48 \times 10^{-8}$ cm s^{-1}) than in the monoculture (average $P_{4\mathrm{kDa,\,mono}} = 1.40 \times 10^{-6} \pm 2.39 \times 10^{-7}$ cm s^{-1}) and biculture cases (average $P_{4\mathrm{kDa,\,bi}} = 1.42 \times 10^{-7} \pm 1. \times 10^{-7}$ cm s^{-1}) at day 5 (Figure 2C); In the triculture cases, various fluorescent model molecules covering a wide range of MW over three orders of magnitude resulted in different permeabilities, suggesting that our engineered BBB features the capability of size-dependent paracellular transport ($P_{376\ \mathrm{Da,\,tri}} = 1.23 \times 10^{-6} \pm 5.01 \times 10^{-7}$ cm s^{-1} and $P_{40\ \mathrm{kDa,\,tri}} = 1.83 \times 10^{-8} \pm 1.60 \times 10^{-8}$ cm s^{-1}), showing approximately 100-fold higher transendothelial permeability for 376 Da fluorescein salt than 40 kDa fluorescein isothiocyanate (FITC)-dextran (Figure 2D). These vascular permeability values are within the range expected for in vivo blood vessels (≈10^{-7} cm s^{-1}),[21–23] indicating that multicellular interactions strengthened the integrity of the vessel to be more impermeable to small molecules, especially in the presence of pericytes. Additionally, considerable angiogenic sprouting was observed in the triculture case (Figure 2E). Conversely, monocultured brain endothelial cells did not show notable capability of organizing new vascular branches within the 3D collagen. However, when we cocultured the brain endothelial cells (bECs) with astrocytes and pericytes, the bECs sprouted from the host liner blood vessel (Figure 2F) and organized new vessels possessing hollow lumens. We verified the existence of perfusable lumens by visualizing them with 4 kDa FITC-dextran (Figure S4, Supporting Information). The cytokine assay confirmed that these enhanced vascular functions (i.e., low transendothelial permeability) and angiogenic sprouts were attributed to the production of pro- (angiogenin, angiopoietin-2, and 4) and anti-angiogenic

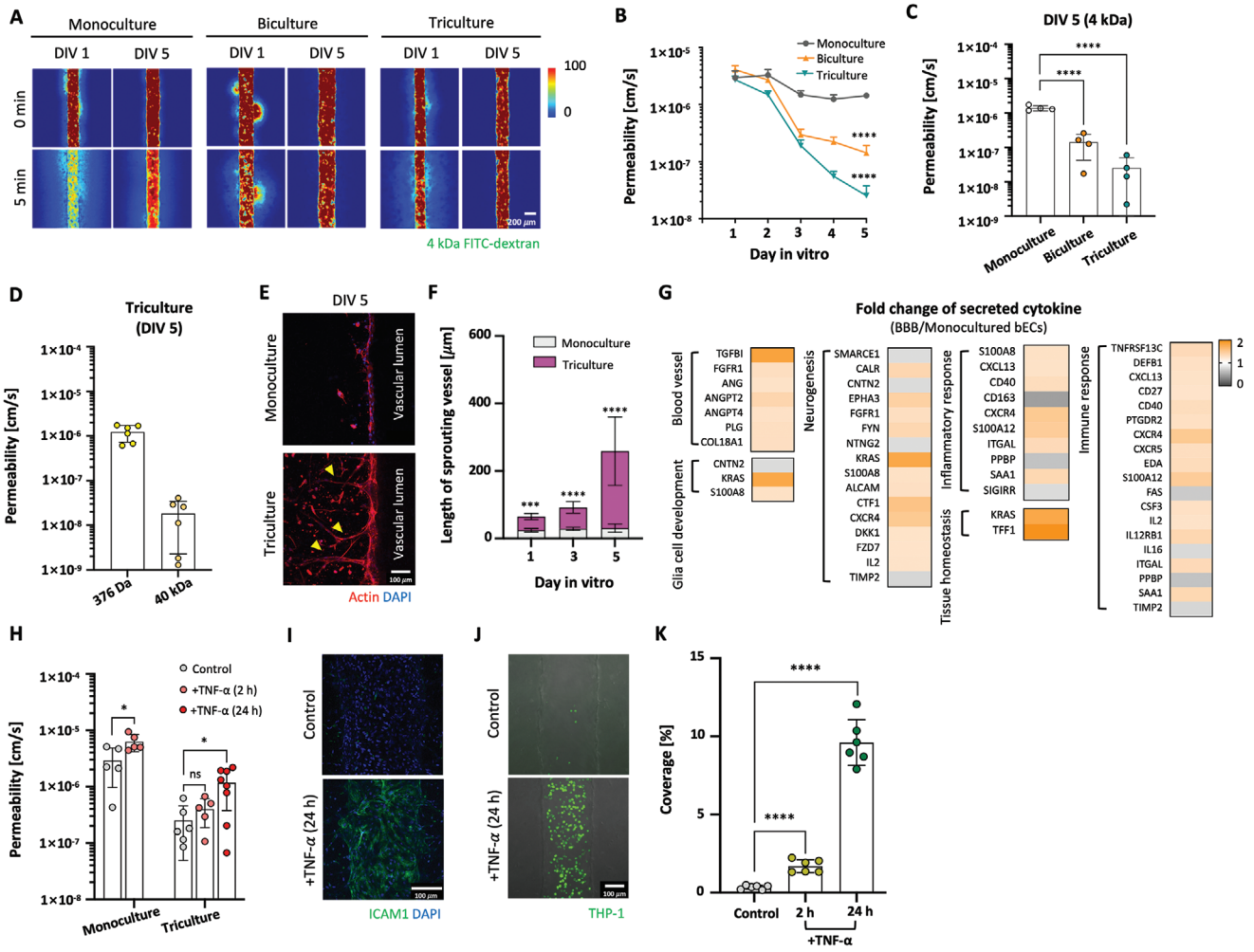

Figure 2. Examination of the functionality of our engineered BBB chip. A) Visualization of leakage of 4 kDa FITC-dextran from the blood vessel. Leakage of dextran significantly decreased in biculture and triculture models compared to monoculture models (monoculture: HBMEC, biculture: HBMEC + HBVP, triculture: HBMEC + HBVP + HA) (scale bar: 200 µm). B) Variation of vascular permeability over a period in culture. A longer culture period lowered the permeability, and C) the lowest value was measured in the triculture condition on day 5 ($n = 4$ for each condition; significance is indicated by **** for $p < 0.0001$; all by unpaired t-test). D) Measurement of vascular permeability of the matured BBB chip on day 5 using fluorescent dyes (376 Da fluorescent sodium salt and 40 kDa FITC-dextran). The permeability was in the range of in vivo value (≈10^{-7} cm s^{-1}) ($n = 6$ for each condition). E) Endothelial sprouting and F) its length variation over a period of culture (scale bar: 100 µm) ($n = 8$ for each condition; significance is indicated by *** for $p < 0.005$ and **** for $p < 0.0001$; all by unpaired t-test). G) Fold change of the secreted cytokines on the BBB chip on day 5. In particular, the secretion of angiogenic growth factors were elevated compared to HBMEC monoculture models. H) Variation of permeability caused by short (2 h) and long-term (24 h) exposure of inflammatory cytokine TNF- α in monoculture and triculture models ($n \geq 5$ for each condition; significance is indicated by * for $p < 0.05$; all by unpaired t-test). I) Expression of the inflammatory marker of endothelial cells (intercellular adhesion molecule-1, green) when exposed to TNF- α (50 ng mL^{-1}, for 24 h) (scale bar: 100 µm). J) Adhesion of human monocytic THP-1 cells (green) in the TNF-α treated vessel (scale bar: 100 µm). K) Coverage of THP-1 cells on the inflammatory endothelium ($n = 6$ for each condition; significance is indicated by **** for $p < 0.0001$; all by unpaired t-test).

factors (angiostatin and endostatin) (Figure 2G).[24] Although the recent study showed that pericytes contributed significantly to stabilizing vascular integrity, leading to low permeability, the capillary sprouting was notable in our system. Kim et al. reported that even in the presence of pericytes, applying luminal flow was crucial for suppressing capillary sprouts.[25] In this study, occasional luminal flow, created by regular media exchanges from reservoirs, instead of continuous shear stress could induce the brain endothelial sprouts into the 3D hydrogel.

We exposed the brain endothelium to tumor necrosis factor-α (TNF-α) (50 ng mL^{-1}), to observe the inflammatory response of our BBB model to external stimuli. Interestingly, the monocultured brain endothelium was easily disrupted by short-term exposure to TNF-α, showing increased permeability (average $P_{con} = 2.91 \times 10^{-6} \pm 1.95 \times 10^{-6}$ cm s^{-1} and $P_{treated,\ 2h} = 6.27 \times 10^{-6} \pm 2.11 \times 10^{-6}$ cm s^{-1}). Conversely, the tricultured endothelium has no significant response to the short-term TNF-α-mediated stimulation. However, the long-term TNF-α stimulation caused vascular dysfunction (average $P_{con} = 2.52 \times 10^{-7} \pm 2.03 \times 10^{-7}$ cm s^{-1}, $P_{treated,\ 2h} = 3.98 \times 10^{-7} \pm 2.12 \times 10^{-7}$ cm s^{-1}, $P_{treated,\ 24h} = 1.17 \times 10^{-6} \pm 7.95 \times 10^{-7}$ cm s^{-1}) in the tricultured BBB models (Figure 2H), which was attributed to the BBB-composing cells (i.e., astrocytes and pericytes) that support and modulate the BBB functionality.[26–28] The elevated expression

of intracellular adhesion molezcules-1 (ICAM-1) (Figure 2I) and adhesion of human monocytic cells (THP-1) in the TNF-α-stimulated brain endothelium (Figure 2J,K) indicates endothelial activation and vascular inflammation.

2.3. Investigation of the Temporary Opening Effect of the BBB

Several techniques for temporal opening of BBB or drug delivery systems that can bypass the transport barrier have emerged as innovative strategies to promote drug delivery through the BBB and neural tissue.[29–31]

We temporarily opened the transport barrier of the engineered BBB using two BBB-opening agents having different opening mechanisms, that is, mannitol and gintonin. Mannitol is used to reduce intracranial pressure, and osmotically opens the BBB by inducing endothelial cell shrinkage.[32] Meanwhile, ginseng-derived gintonin binds to the lysophosphatidic acid (LPA) receptors of the cells, and ultimately opens the BBB through LPA-induced Rho-pathway activation.[33] Both agents increase the permeability, and facilitate molecular transport from blood vessels (**Figure 3**A).

The matured BBB (day in vitro 5) was exposed to both agents (mannitol: 1 M, gintonin: 10 μg mL^{-1}) for 60 min, and its opening effect was verified by comparing the permeability of 4 kDa FITC-dextran solution. As expected, the leakage was significantly increased in the groups treated with mannitol or gintonin ($P_{+\text{mannitol}} = 4.27 \times 10^{-6} \pm 7.94 \times 10^{-7}$ cm s^{-1}, $P_{+\text{gintonin}} = 2.96 \times 10^{-7} \pm 7.63 \times 10^{-7}$ cm s^{-1}) compared to the control group ($P_{-\text{mannitol}} = 2.77 \times 10^{-7} \pm 4.08 \times 10^{-7}$ cm s^{-1},

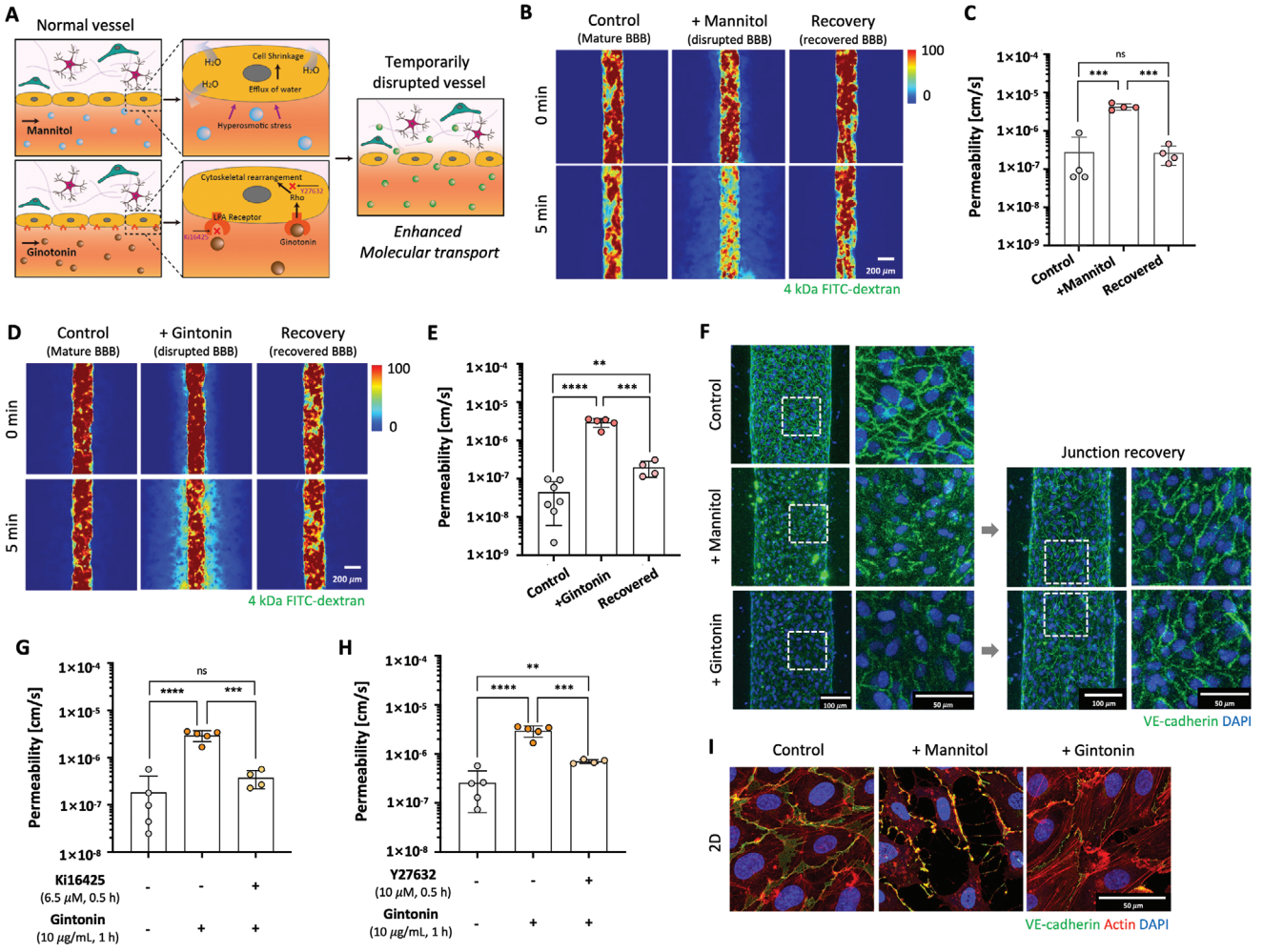

Figure 3. Temporary opening effect of the BBB using BBB-opening agents (mannitol and gintonin) A) Schematic of BBB opening procedure by mannitol and gintonin and enhanced molecular transport across the opened BBB. B) Leakage of 4 kDa FITC-dextran from the mannitol-treated and recovered vessels (scale bar: 200 μm). C) Estimated permeability of the mannitol-treated and recovered vessel ($n = 4$ for each condition; significance is indicated by *** for $p < 0.005$; all by unpaired t-test). D) Leakage of 4 kDa FITC-dextran from the gintonin-treated and recovered vessels (scale bar: 200 μm). E) Estimated permeability of the gintonin-treated and recovered vessel ($n \geq 4$ for each condition; significance is indicated by ** for $p < 0.01$, *** for $p < 0.005$, and **** for $p < 0.0001$; all by unpaired t-test). (F) Opening and recovery of adherens junction (VE-cadherin, green) when the BBB was temporarily opened by mannitol (middle) and gintonin (bottom) (scale bar: 100 μm). G,H) Inhibition of gintonin-mediated BBB opening. Pretreatment of the G) LPA receptor antagonist (Ki16425) and H) Rho kinase inhibitor (Y27632) suppressed gintonin-mediated BBB opening ($n \geq 4$ for each condition; significance is indicated by ** for $p < 0.01$, *** for $p < 0.005$, and **** for $p < 0.0001$; all by unpaired t-test). I) Cytoskeleton (actin, red) of the endothelial cells. Alignment of actin filaments in gintonin-treated endothelial cells (scale bar: 50 μm).

$P_{-\text{gintonin}} = 4.79 \times 10^{-8} \pm 4.42 \times 10^{-8}$ cm s^{-1}) (Figure 3B–E). Moreover, the expression of VE-cadherin, which is an adherens junction protein in brain endothelial cells, decreased without cell detachment when these cells were exposed to both mannitol and gintonin (Figure 3F). Specifically, the alignment and bundling of actin filaments were observed in gitonin-treated brain endothelial cells (Figure 3I). Both agents showed a concentration-dependent BBB-opening effect. The mannitol induced time-dependent opening of the BBB, with the maximum opening at 30 min; thereafter, the effect was saturated (Figure S5, Supporting Information). The permeability (Figure 3C,E) and junctional protein (Figure 3F) of the BBB recovered in about 24 h after the removal of agents ($P_{+\text{mannitol, recovered}} = 2.64 \times 10^{-7} \pm 1.38 \times 10^{-7}$ cm s^{-1}, $P_{+\text{gintonin, recovered}} = 1.98 \times 10^{-7} \pm 8.91 \times 10^{-7}$ cm s^{-1}), indicating that the temporal opening of the BBB did not exhibit any significant toxicity. Although we performed experiments associated with the recovery after the temporary opening of BBB under identical conditions for comparative analysis of the two opening agents, recovery time (i.e., a time frame of the temporary opening) for gintonin could have been slightly longer than 24 h based on a statistical assessment. The gintonin-induced change was blocked by pretreating the engineered BBB with Ki16425 (LPA receptor antagonist, 6.5 μM) and Y27632 (Rho kinase inhibitor, 10 μM) for 30 min, to verify the gitonin-mediated opening pathway. As expected, the pretreatment with Ki16425 and Y27632 blocked the gintonin-associated changes of the brain endothelial cells, and eventually neutralized the BBB-opening effect (Figure 3G,H). We expect opening the BBB using these materials would minimize adverse effect such as massive extravasation of cells and neuronal damage caused by overdosing microbubble and thus excessive stimulus (e.g., instantaneously detrimental local pressure) generally observed in focused ultrasound (FUS)-induced BBB opening process.[34–37] Additionally, as shown in Figure 3 and Figure S5, Supporting Information, our chips enabled investigating the BBB opening effect depending on agent's concentration and exposure time, and reversibility of loosened BBB. These results render that control of vascular permeability and prediction of BBB opening effect become available in preclinical trial with our engineered BBB chip before animal studies. Eventually, we expect that the utilization of the BBB chips saves time and cost and allows minimal use, if necessary, of animal models by determining optimal dosages range preventing adverse effects.

2.4. Modeling of In Vitro Human GBM Model

Next, we applied the proposed model on a physiological level, and investigated the effect of the interaction of the BBB and human GBM on drug responsiveness and delivery (**Figure 4**A). Moreover, we embedded GBM spheroids in our BBB chip to replicate more physiologically relevant TMEs,[3,38] because TMEs and several characteristics of the GBM influence tumor progression and drug resistance.

Two types of human glioblastoma cell lines, including T98G (TMZ-resistant cells) and U87MG (TMZ-sensitive cells), were used to validate the potential of the proposed platform as a disease model.[39] Both cell lines were cultured on 3D SpheroFilm microwells at a density of 4×10^5 cells mL^{-1} for 3 days, to promote the organization of the GBM spheroids. Each spheroid was isolated and labeled using CellTracker Green for easier fluorescence live cell imaging. Then, a mixture of GBM spheroid and collagen type I solution (3 mg mL^{-1}) was injected into the hollow side channel (with a diameter of 550 μm) after the maturation of BBB (DIV 5) (Figure S1(iv,v), Supporting Information). Moreover, the distance between the tumor spheroids and brain endothelium was consistently maintained at ≈1 mm, because the GBM spheroids were introduced through the predefined microchannel throughout the repetitive experiment.

Interestingly, both tumor cells invaded the collagen space, showing different migratory patterns (Figure S6A, Supporting Information). T98G cells collectively migrated by maintaining cell-to-cell contact; however, U87MG cells spread at a single-cell level with a 2.2 increase in the invasive distance (Figure S6B, Supporting Information). These different behaviors are attributed to distinct tumorigenic abilities associated with growth, metastasis, and metabolism. Additionally, U87MG cells are more invasive, and consume more glucose than T98G cells according to a previous report.[40] These results suggest that our chip has potential applications in personalized medicine, and patient-derived cancer cells can be used in our chip to identify patient-specific characteristics for further research.

2.5. Tumor-Induced Changes of the Brain Blood Vessel

Tumors are known to drive structural and functional changes in the blood vessel, such as hyperpermeability, formation of new angiogenic vessels, and instability.[41,42] We also investigated whether cocultured GBM spheroids caused vascular changes or dysfunction.

In the absence of a tumor, new angiogenic vessels were barely generated, and there was no preferred direction in the branching from the pre-existing linear vessel. However, in the presence of a tumor, we observed significant endothelial sprouting toward GBM spheroids with increased length and number of angiogenic vessels (Figure 4C,D). Additionally, we observed that the blood vessel became dilated a day after the GBM spheroid was added to the chip. Furthermore, we measured the vascular diameter of the BBB and GBM chips on day 9 (Figure 4E), and then, acquired the vascular change value by dividing these diameters by the vascular diameter at day 5, to quantify the vascular variation during the culture period. Consequently, the blood vessels were significantly enlarged in the presence of GBM spheroids for 4 days (Figure 4F). The vascular permeability increased ($P_{\text{BBB chip}} = 2.54 \times 10^{-8} \pm 2.48 \times 10^{-8}$ cm s^{-1}, $P_{\text{tumor chip}} = 1.43 \times 10^{-7} \pm 7.29 \times 10^{-8}$ cm s^{-1}) within the range of in vivo blood vessels (≈10^{-7} cm s^{-1}) (Figure 4G,H). The expression of ICAM1 on the vessels was also partially detected in the tumor chips (Figure 4I). These changes may be due to the secretion of cytokines that are associated with tumor angiogenesis, including cyclooxygenase (PTGS2), apelin receptor (APLNR), bone morphogenic protein 2 (BMP2), heparin-binding epidermal growth factor, and interleukin 34 (IL-34),[43–47] from the GBM (Figure 4J). In particular, the apelin/APJ system is known to be related to the activation of nitric oxide (NO), resulting in the dilation of blood vessels and the release from endothelial cells.[48–50]

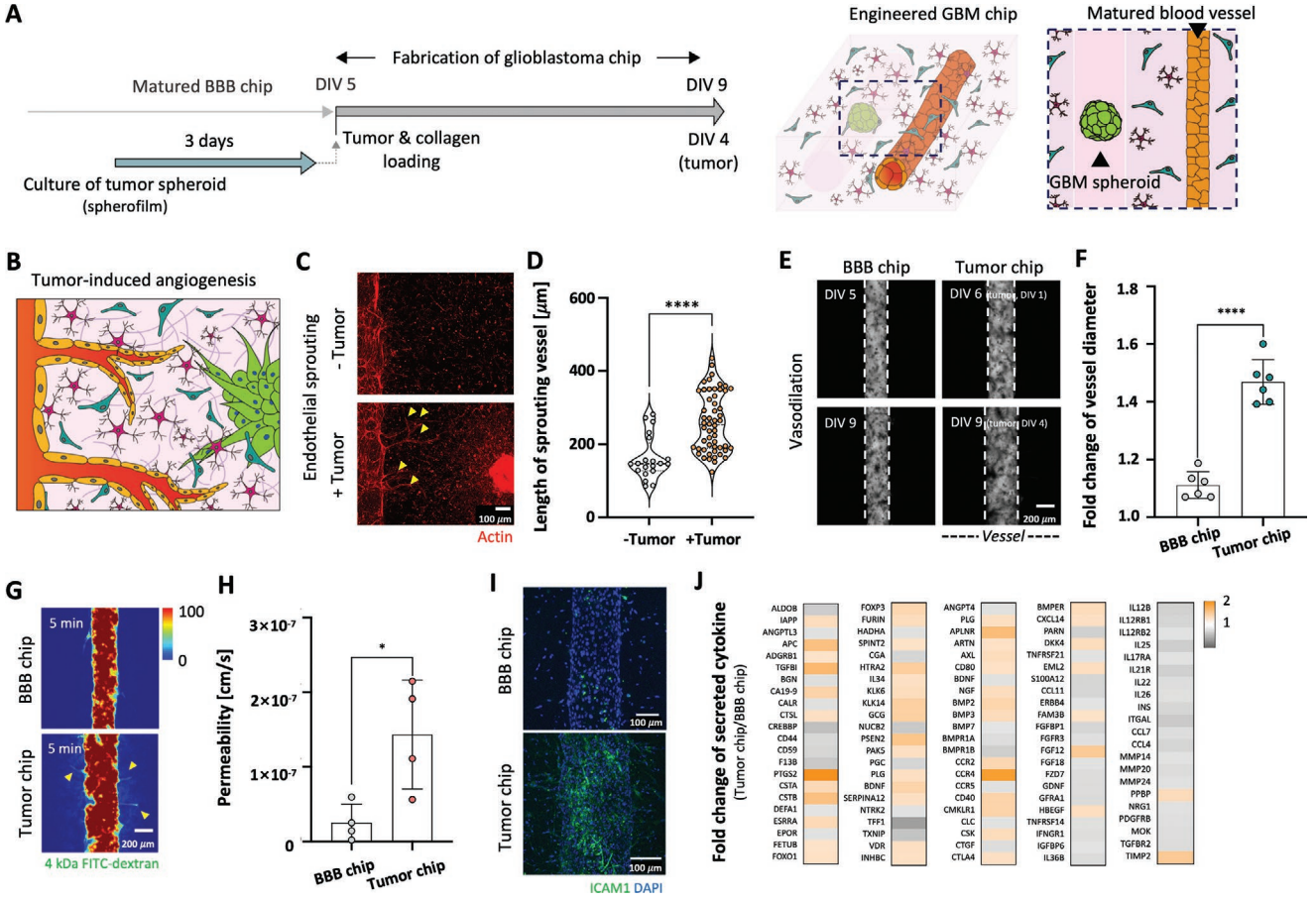

Figure 4. GBM-induced structural and functional change of the vasculature. A) Timeline for fabrication of in vitro human glioblastoma chips. B) Schematic of tumor-induced angiogenesis. C) Formation of new vessels (yellow arrow) from pre-existing vessel toward the GBM spheroid (scale bar: 100 μm). D) Length and number of neo-vessels toward the GBM spheroid were quantified ($n > 20$ for each condition; significance is indicated by **** for $p < 0.0001$; all by unpaired *t*-test). E) Tumor-induced vascular dilation (scale bar: 200 μm). F) Fold change of the vascular diameter of the BBB and tumor chips on day 9 with respect to the BBB chip on day 5 ($n = 6$ for each condition; significance is indicated by **** for $p < 0.0001$; all by unpaired *t*-test). (G) Comparison of the leakage of 4 kDa-FITC dextran from the BBB and tumor chips on day 9 (scale bar: 200 μm). H) Quantified value of vascular permeability of the BBB and tumor chips ($n = 4$ for each condition; significance is indicated by * for $p < 0.05$; all by unpaired *t*-test). I) Expression of ICAM1 (green) in the BBB chips (day in vitro 5) and tumor chips (day in vitro 9) (scale bar, 100 μm). J) Fold change of the secreted cytokines in the tumor chips on day 9 with respect to the BBB chips on day 5.

2.6. Monitoring of the Morphological Change and Behavior of the Tumor

T98G cells showed different morphologies and growth patterns depending on the culture environment. In particular, they exhibited a rounded shape when the GBM spheroids were cultured without BBB, representing a low level of invasion (**Figure 5**A). However, co-culturing with BBB-composing cells made the tumor cells more invasive and aggressive with higher growth rates (Figure 5B) and elongated morphologies (Figure 5C,D). Considering that the GBM spheroids cultured in the BBB-conditioned medium collected from the BBB chips at day 5 showed similar morphological changes and growth patterns to the GBM in the tumor chip, the behaviors of tumor cells, such as the process of invasion and metastasis, are affected by neighboring cells through paracrine effects. We collected the supernatants from monocultured ($n = 5$) and cocultured ($n = 5$) GBM chips to compare the level of secreted cytokines with the culture conditions. An increasing production of cytokines associated with tumor invasion and growth, including interleukin cytokines (IL-2, 5, 6, 7, 10, 13, 15, and 21), was observed from the cytokine array analysis (Figure 5E).[51,52] Additionally, we investigated the effect of vessel structure nearby on brain tumor growth by intentionally eliminating the collagen channel around GBM spheroid (Figure S7A, Supporting Information). Brain tumor cells' morphologies showed similarly elongated shape (Figure S7B, Supporting Information); however, the invasion distance of tumor cells more sharply increased in the presence of vessel structure than in the absence (Figure S7C, Supporting Information). The size of the brain tumor spheroid, including invading tumor cells, was also more extensive when the vessel structure existed nearby (Figure S7B, Supporting Information). These results was attributed to enough supply of nutrient and removal of wastes: similarly, the importance of delivery and drainage channels on the microcirculation system was reported elsewhere.[53] Overall, both multicellular interactions and perfusable vessels nearby (i.e., geometrical structure) significantly influence the brain tumor's invasion and progression.

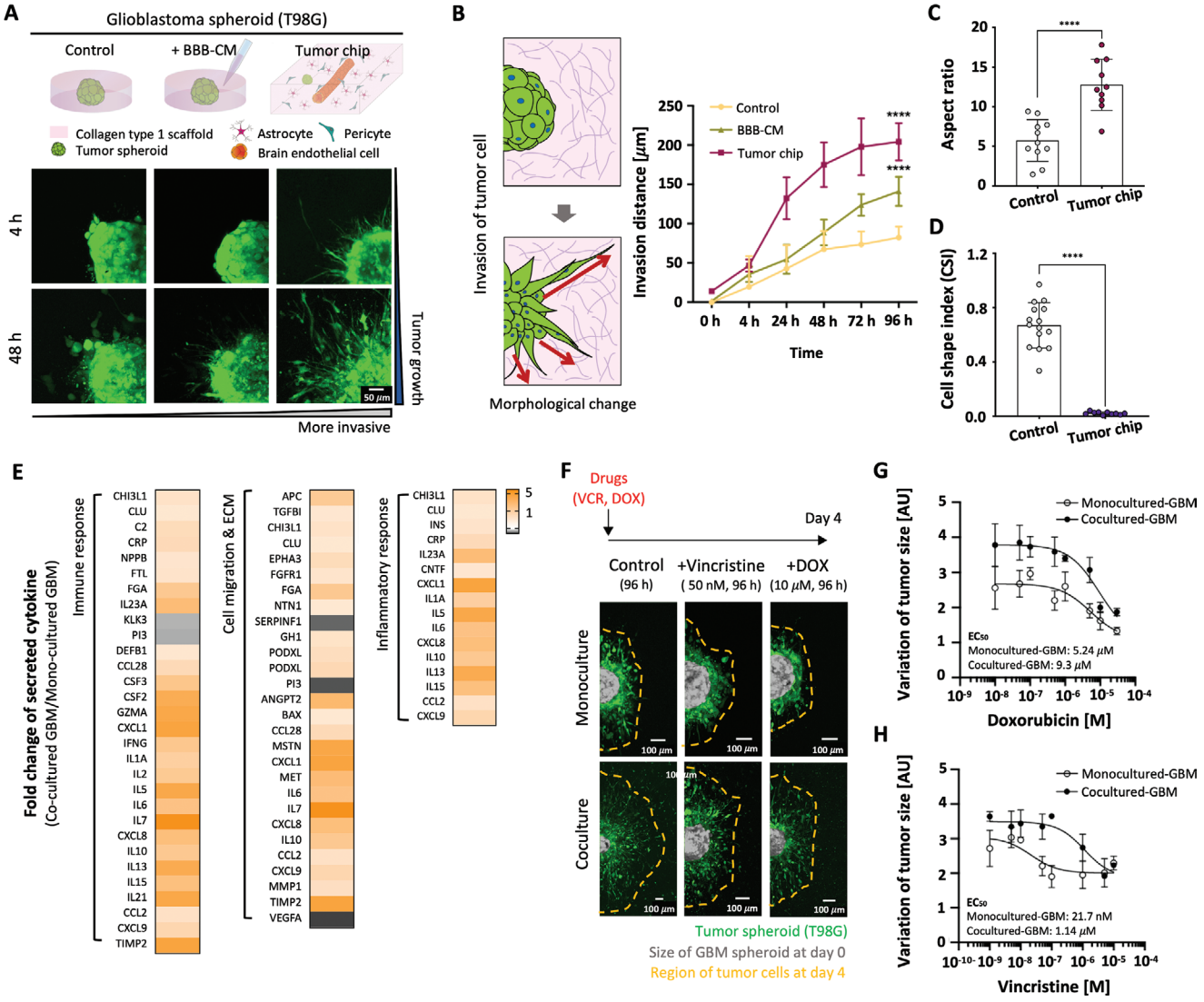

Figure 5. Fabrication of human glioblastoma chip and tumor cell behavior. A) Different growth pattern of GBM spheroid (T98G) depending on the culture conditions (monoculture versus monoculture in BBB-conditioned medium versus coculture with BBB-composing cells) (scale bar: 50 μm). B) Change in tumor spheroid invasion. In the physiologic tumor environment, the tumor cells showed more aggressive morphologies with high invasive capacity ($n = 10$ for each condition; significance is indicated by **** for $p < 0.0001$; all by unpaired t-test). C,D) Characterization of morphological change of the GBM: C) aspect ratio and D) cell shape index (bottom) ($n \geq 10$ for each condition; significance is indicated by **** for $p < 0.0001$; all by unpaired t-test). E) Fold change of the secreted cytokines associated with immune response, cell migration, and inflammation on the tumor chips with respect to monocultured GBM. F) Variation of the tumor region in response to anticancer drug (DOX and VCR) treatment. The tumor region on day 4 (yellow dotted line) was divided by the initial tumor size on day 0 (gray region) (scale bar: 100 μm). G,H) Dose-response curve with EC50 values of G) DOX and H) VCR of monocultured GBM and cocultured GBM ($n \geq 3$ for each condition).

2.7. Assessment of Anticancer Drugs Response of GBM Spheroid

Chemotherapeutic agents used to treat glioblastoma can be classified according to their BBB penetrating ability. Temozolomide (TMZ) can easily penetrate across the BBB owing to its small molecular weight (194.15 g mol^{-1}) and lipophilic property, while vincristine (VCR) and doxorubicin (DOX) are BBB-nonpenetrant owing to their relatively large size (VCR: 824.958 g mol^{-1}, DOX: 543.52 g mol^{-1}).[54–56] First, we investigated the growth inhibition effect caused by the drugs, depending on the BBB–GBM coculture conditions. Then, we measured the size of the GBM spheroids (T98G; TMZ-resistant) at days 0 and 4, and obtained a relative level of tumor growth change for each group after introducing these anticancer drugs through the luminal structure of the BBB, mimicking the in vivo drug administration (Figure 5F). We found that a higher concentration of drugs was required to induce an identical inhibition effect in the GBM–BBB interaction case compared to the GBM only case. The EC_{50} (the effective concentration of a drug exhibiting the half-maximal effect) values of the VCR and DOX, observed in the GBM cocultured with the BBB structure ($EC_{50\text{-VCR}} = 1.14$ μM, $EC_{50\text{-DOX}} = 9.3$ μM), were 52.53 times (VCR) and 1.77 times (DOX) fold

higher than the monocultured GBM case ($EC_{50\text{-}VCR}$ = 21.7 nM, $EC_{50\text{-}DOX}$ = 5.24 μM) (Figure 5G,H). It was thought that the transport of VCR, which has a larger molecular weight than DOX, was relatively strongly impeded by blood vessels. To validate the effect of blood vessel tightness on drug delivery, we also monitored DOX uptake in GBM spheroids and the growth pattern of tumor cells for 4 days in BBB-intact and BBB-opened models. In the early stage of drug exposure, in which DOX did not present a cytotoxic effect, we observed higher uptake of DOX in GBM spheroids in the BBB-opened model due to facilitated delivery through loosened BBB. However, we found that the uptake level of DOX in both groups became similar after 24 h due to the DOX-induced BBB disruption (Figure S9A,B, Supporting Information). Since the DOX rapidly diffused in the BBB-opened model, the tumor growth rate was retarded for up to 72 h. However, such differential effect disappeared at 96 h because the DOX was entirely transported through the DOX-damaged BBB structure. Furthermore, the nonspecific uptake of DOX by nontumorous cells (i.e., astrocytes and pericytes; Figure 7E and Figure S11, Supporting Information) can also contribute to the increased EC50 value.

These results indicate that physical barriers hinder drug delivery and cellular interactions, causing the tumor cells to become more resistant to drugs. We also showed the growth inhibition of the TMZ-sensitive GBM spheroids (U87MG) by the BBB-penetrated TMZ (Figure S6C,D, Supporting Information).

2.8. Investigation of the Role of WNT/β-Catenin Signaling in GBM

We isolated the GBM spheroids from the tumor chip on day 9 (tumor, on day 4), as shown in Figure S8B, Supporting Information, to analyze the RNA expression profiles. In our tumor chip, the tumor spheroids can be harvested in an embedded form in the hydrogel with the microchannel shape, by mechanically irritating the interaction between the host and guest hydrogels. Furthermore, other cells such as BBB-composing cells were excluded in the retrieval process, allowing the biological analysis of the cultured GBM under the BBB–GBM interaction. We found that the GBM cocultured with BBB-composing cells changed the gene expression associated with WNT/β-catenin signaling, which is a well-known pathway associated with tumor progression. The dysregulation of this pathway in tumors makes the cells more invasive and resistant to the drugs by inducing epithelial-to-mesenchymal transition (EMT) with an altered expression of WNT signaling-related genes (**Figure 6**A).[57–59] Coculture with BBB-composing cells upregulated the expression of WNT family member 5A (WNT5A, WNT ligand), Frizzled2 (FZD2, WNT receptor), and transcription factor 4 (TCF4), and downregulated the expression of lymphoid enhancer-binding factor 1 (LEF1, WNT pathway inhibitor). WNT5A is known to stimulate the migration of glioma cells and induce greater drug resistance.[60,61] Compared to monocultured GBM, cocultured GBM expressed high levels of cell surface

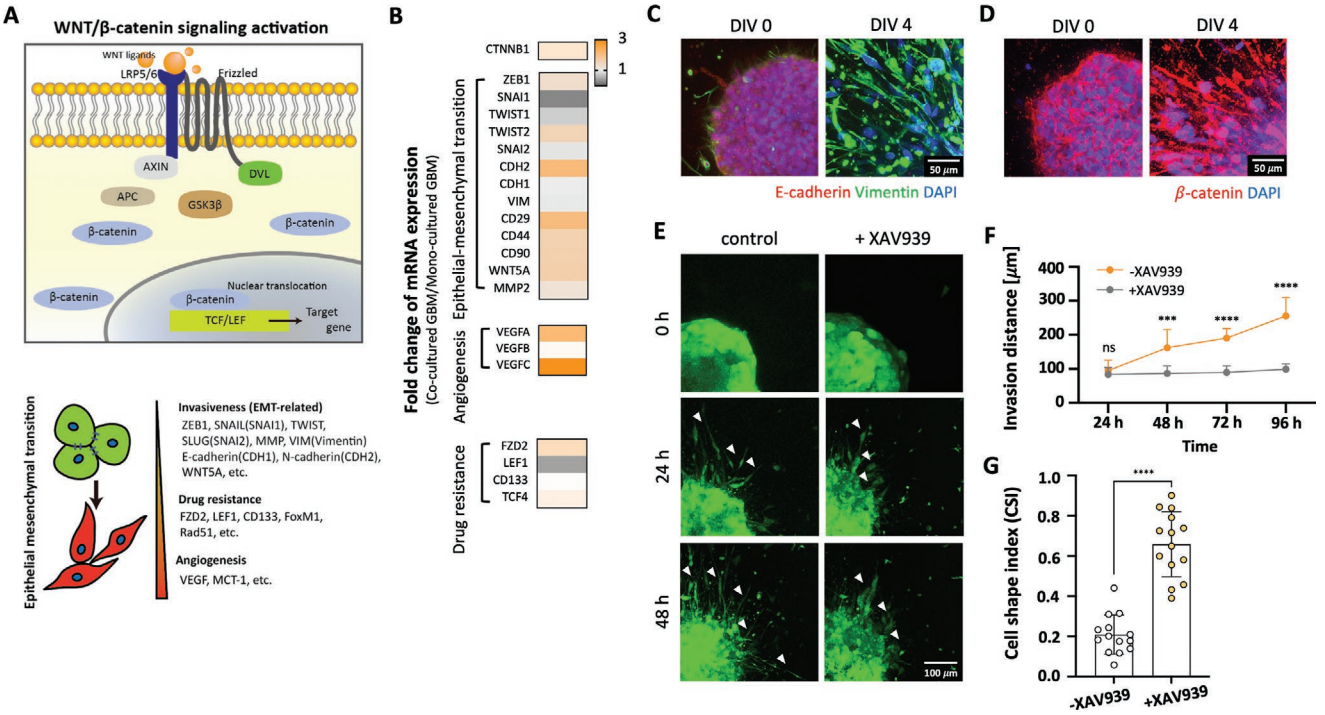

Figure 6. WNT/β-catenin signaling pathway in GBM. A) Overview of WNT/β-catenin signaling activation. Activated WNT pathway induced the EMT of glioblastoma to be more invasive and resistant to drugs. B) Fold change of gene expression in the cocultured GBM with respect to the monocultured GBM. C) Expression of EMT-related markers (epithelial marker: E-cadherin, mesenchymal marker: Vimentin) in the cocultured GBM on days 0 and 4 (scale bar: 50 μm): D) Expression of β-catenin in the cocultured GBM on days 0 and 4 (scale bar: 50 μm). E–G) Blockage effect of WNT-signaling by XAV939. E) When treated with XAV939, the behavior of the GBM changed (scale bar: 100 μm). Inhibition of the WNT-signaling decreased F) the invasion distance of the GBM and altered G) their morphology to a nonaggressive shape ($n \geq 10$ for each condition; significance is indicated by *** for $p < 0.005$ and **** for $p < 0.0001$; all by unpaired t-test).

receptors associated with mesenchymal stem cells, including CD29, CD44, and CD90. Moreover, the expression of vascular endothelial growth factor A and C (VEGFA, VEGFC), which are responsible for tumor angiogenesis, increased (Figure 6B). We also visualized the EMT of the GBM spheroids by staining EMT markers (E-cadherin, epithelial marker, vimentin, and mesenchymal marker). During EMT, the E-cadherin was downregulated, and the vimentin was highly expressed in the invading tumor cells (Figure 6C). The activation of EMT also alters the localization of catenin beta-1, known as β-catenin, which is a key mediator of the WNT pathway.[62] In the WNT-off stage, β-catenin was highly localized at the cell membrane, maintaining its intact sphere structure before invading the collagen at day 0; however, the EMT (WNT-on stage) led to an accumulation of β-catenin in the cytoplasm (Figure 6D). This finding suggests that multicellular environments must be mimicked in preclinical in vitro models to accurately predict the therapeutic effect, as the TME induced the genetic alteration of the tumor cells to be more drug resistant. We blocked the WNT signaling with XAV939 (10 μM) and monitored the behavior of the GBM spheroid (Figure 6E), to validate the WNT pathway-dependent invasion of the GBM spheroid. When WNT signaling was blocked, the invasion of the GBM spheroid was significantly inhibited, showing round shaped morphology (Figure 6F,G). Blocking the WNT signal caused an anticancer effect with a significant growth inhibitory effect similar to the DOX with less toxicity (Figure S10A,B, Supporting Information).

2.9. Enhanced Delivery of BBB-Nonpenetrant Drugs through the Temporarily Opened BBB

We evaluated the effect of the combinatorial administration of BBB-opening agents (mannitol and gintonin) and BBB-nonpenetrant drugs (DOX), to address and overcome the limited delivery of drugs through the BBB. Notably, long-term exposures to DOX (10 μM for 4 days) induced cellular death in our chips (Figure S10C, Supporting Information). Additionally, we found that an optimal condition had to be set for accurately verifying the effect of the BBB-opening agents in drug delivery. In terms of the DOX-induced BBB damage, the viability of the endothelial cells in the BBB was significantly reduced as the exposure time of the DOX increased (**Figure 7**A), and the permeability of the BBB has significantly increased after 9 h of exposure to DOX (Figure 7B). The cytotoxic effects of DOX on the viability and permeability of the blood vessels were not detected for short-term exposures, indicating that long-term exposures are not a suitable for investigating the drug delivery efficiency of DOX. Therefore, the DOX was infused into the endothelium for 3 h, washed, and incubated with fresh medium, to avoid the adverse effects of the drugs. We pretreated the vessel with the BBB-opening agents (mannitol (1 M) and gintonin (10 μg mL^{-1})) for 1 h; then, a process similar to that mentioned above was performed (Figure 7C) to enhance drug transport across the blood vessel. Exposure to the DOX (3 h), with the pretreatment of both BBB-opening agents, did not induce the death of the brain endothelial cells (Figure 7D). We measured the release of DOX through the opened BBB with fluorescence intensity, and acquired the uptake level of DOX within the GBM spheroids. Notably, the DOX was rapidly delivered to the perivascular space in 30 min when the BBB was temporarily opened, as shown in the DOX (red signal)-uptake cells, compared to the normal blood vessel (Figure 7E). The accelerated delivery of DOX also significantly increased the uptake of DOX within the GBM spheroids after 3 h (Figure 5F,G). Eventually, in the BBB-opened models, we confirmed that the rapid delivery of DOX resulted in a more rapid inhibitory effect on tumor proliferation in 48 h (Figure S9C, Supporting Information).

3. Discussion

Various vascularized tumor models have been developed and can be classified into three types: micropost-based hydrogel patterning,[11,13,63,64] porous membrane-based multilayered structure,[65,66] and removal of templates from gelated hydrogels.[67] Furthermore, direct writing of 3D BBB structures were also proposed by using two-photon lithography.[68] These models have been based on utilizing HUVECs, HLFs, and cancer cell lines in fibrin-based hydrogels without brain-originated cells or with animal cells, making them unsuitable for modeling human brain-specific tumors.[11–14,68–70] Furthermore, the structure, cellular components, and barrier functions of the brain blood vessel is different from those of the blood vessels in other tissues.[26] In this study, we fabricated a BBB model with a perfusable cylindrical vessel by removing microneedles from the gelated hydrogel to better control the vascular dimension and systematically measure transendothelial permeability assay. Although many studies have simulated the barrier function of the BBB and proved its selective permeability,[25,68,70–77] the application of a BBB model in vitro to brain tumors has drawn little attention. To precisely model the brain tumor microenvironment, we used human brain-specific cells (i.e., human brain microvascular endothelial cell, human astrocyte, and human brain vascular pericyte) and validated BBB functionality before applying our engineered BBB to the GBM models. The vascular structure embedded within the soft hydrogel matrix can dynamically remodel the surrounding matrix biochemically and structurally, confirmed by the deposition of collagen type IV and laminin (Figure 1I), and dilation in the presence of tumor spheroids (Figure 4E,F). Therefore, this platform is suitable for analyzing changes in the BBB structure and function in response to the solid GBM.

We incorporated GBM spheroids in the form of spheroid-in-hydrogel on DIV5 for a sufficiently long time, to promote the maturation of the BBB structure through the side channel. The incorporation of the GBM spheroids after BBB maturation does not affect early stage blood vessel formation. Furthermore, the distance between the GBM spheroid and brain microvasculature can be controlled throughout the repetitive experiments, as the GBM spheroid is introduced through predefined channels, enabling a reliable investigation of the GBM–BBB interaction. During the occurrence and progression of GBM, dynamic interactions with the BBB constituents influence the GBM cell phenotypes.[78] In particular, astrocytes are essential in modeling the GBM environment because activated astrocytes around the GBM promote WNT/β-catenin signaling and their invasion.[79,80] Endothelial cells and pericytes are also known

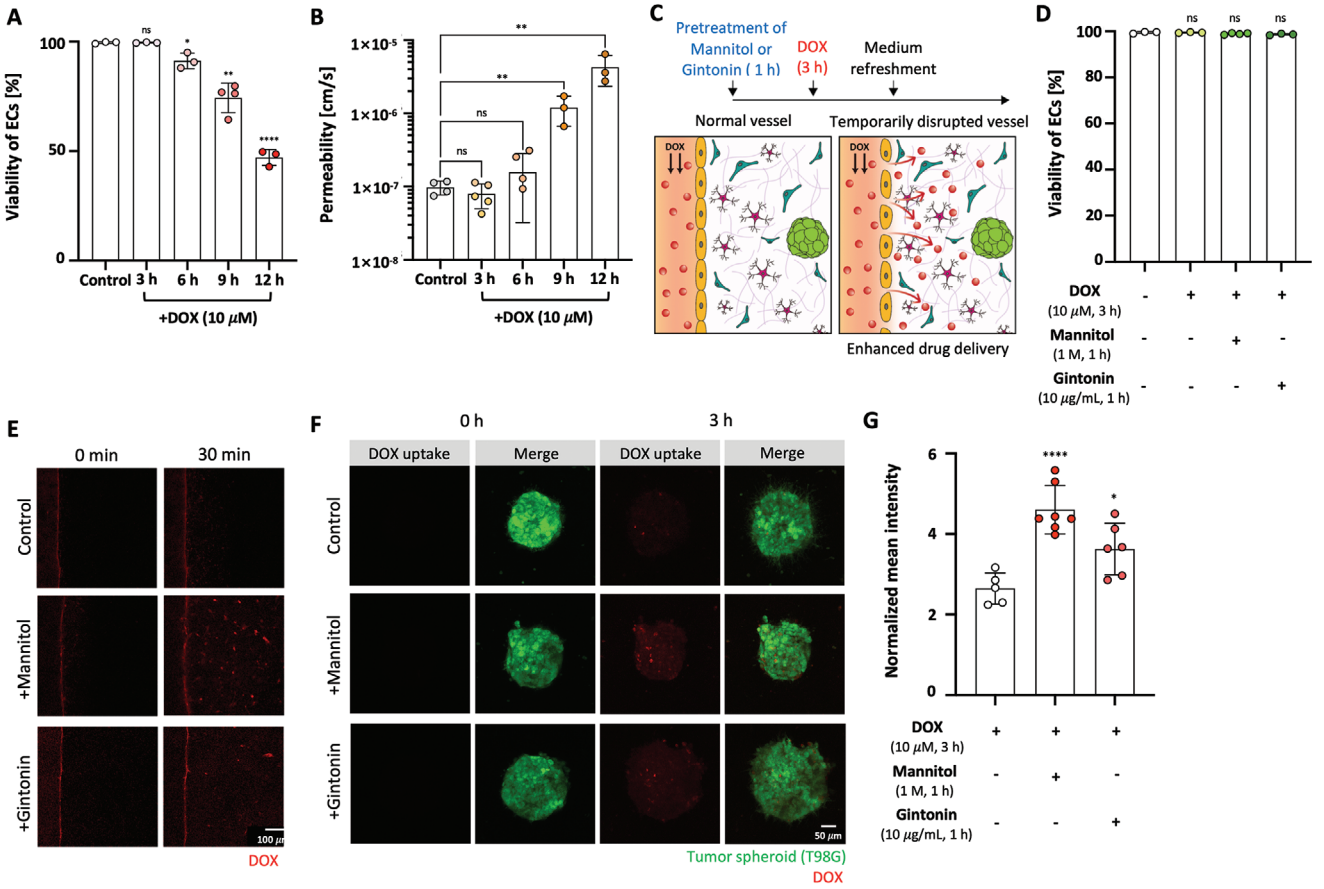

Figure 7. Verification of the combination effect of the BBB-nonpenetrant drug and BBB-opening agent on the chip. A,B) Vascular toxicity caused by the DOX. Effect of DOX (10 μM) on A) viability and B) permeability of the blood vessel. The cytotoxicity of the blood vessel was proportional to the exposure time of the DOX ($n \geq 3$ for each condition; significance is indicated by * for $p < 0.05$, ** for $p < 0.01$, and **** for $p < 0.0001$; all by unpaired *t*-test). C) Schematic of the experimental design to enhance the DOX delivery to the GBM without vascular cytotoxicity corresponding to D) the viability of the blood vessel ($n \geq 3$ for each condition). Pretreatment with mannitol and gintonin enhanced E) DOX delivery from the blood vessel (scale bar: 100 μm) and F) cellular uptake (scale bar: 50 μm). G) Relative fluorescence intensity of the DOX inside the GBM spheroids ($n \geq 5$ for each condition; significance is indicated by * for $p < 0.05$ and **** for $p < 0.0001$; all by unpaired *t*-test.

to enhance the migration of tumor cells by secreting various molecules, such as metalloproteinases (MMPs) and interleukin family cytokines.[78,81,82] The GBM spheroid can be retrieved after paracrine-mediated communication with BBB-composing cells for further biological analysis. Indeed, the GBM cells showed remarkable changes in mRNA levels, especially drug resistance, angiogenesis, and EMT (Figure 6B). Moreover, the cellular components of the TME are critical in the progression and drug responsiveness of tumor cells, as shown in the experimental results of aggressive invasion and EMT-mediated drug resistance. Previous studies have indicated that tumor cells interact with TME-acquired genetic alterations to be more invasive and resistant to drugs.[3,4,38,83]

Additionally, the BBB, which is a unique property in the TME of GBM, physically hinders the transport of drugs and even pumps them out from the perivascular niche.[78,84,85] Our chips can be used for drug delivery studies of central nervous system (CNS)-related diseases. Several approaches, such as the temporary opening of the BBB or bypassing of the delivery barrier, have been studied to overcome the poor penetration of drugs across the BBB.[29–31,54] Although animal models are widely used, these models are not cost efficient, cannot monitor drug delivery in real time,[86] and have concerning ethical issues that limit their utilization in preclinical validation. This indicates the necessity of reliable alternative in vitro models. Our GBM–BBB chip is cost-effective, is employed ethically, and contains in vivo-like characteristics and functionality. We verified the effect of combinatorial administration of BBB-nonpenetrating drugs and BBB-opening reagents, to demonstrate the applicability of our GBM–BBB chip for drug delivery studies. The enhanced delivery across the temporarily opened BBB and the uptake of BBB-nonpenetrating drugs into the GBM were monitored under a microscope in real time. It is expected that the effectiveness of various drugs and combined therapies can be validated using our chips.

We proposed a human cell-based BBB chip, confirmed its in vivo BBB-like functionality through a permeability assay, and showed the importance of triculture in the recapitulation of the barrier function. Temporal opening and subsequent recovery were also exhibited, which is important for testing drug delivery issues. Additionally, we demonstrated that the interaction of BBB and GBM significantly alters both BBB functionality and GBM phenotypes as well as the effectiveness of co-administrating

BBB-opening agents and drugs for overcoming the transport barrier, by incorporating the GBM spheroids after the maturation of the BBB. Additionally, we expect our models to serve as a powerful tool for companion diagnostics and personalized medicine by using patients-derived cells and tumor organoids. Moreover, the technique of isolating only tumor spheroid from the cocultured chips, which is one of the key characteristics, is promising in analyzing the biological characteristics of the tumor and predicting their responses to drugs. Therefore, we believe that our BBB and GBM chips can serve as robust in vitro platforms in translational medical science to study the mechanisms of CNS diseases and drug discovery and screening.

4. Experimental Section

Fabrication of the Microfluidic Device: Sylgard 184 PDMS (SYLGARD 184 silicone elastomer; Dowhitech Co., Gyeonggi, Korea) was mixed with a curing agent at a ratio of 10:1; poured into the mold with microneedles having diameters of 550 and 235 µm (DASAN Cut, Gyeongbuk, Korea); and then, polymerized at 80 °C for 3 h. Subsequently, the needles were removed from the cured PDMS, which was punched with a rectangular hole (4 × 10 mm), and then, bonded to the unpatterned PDMS layer with a thickness of 1 mm via oxygen plasma treatment (CUTE-1MPR, Femto Science Co., Gyeonggi, Korea). The integrated PDMS layer was punched with circular holes (six reservoirs: 8 mm, two collagen injection ports: 1 mm) to create medium reservoirs and collagen injection ports. The microneedles were injected into the PDMS channel again, and then, bonded to the glass slide via oxygen plasma treatment. A detailed process for chip fabrication was reported in a previous study.[87] The chamber was sequentially filled with 2 mg mL^{-1} dopamine hydrochloride dissolved in 10 mM tris-HCl buffer (pH 8.5) for 3 h,[88] to prevent collagen detachment from the PDMS surface. Then, the dopamine solution was aspirated, and the chamber was washed twice with phosphate-buffered saline (PBS).

Cell Culture: HBMECs were purchased from ScienCell (San Diego, CA, USA) and Cell Systems (Kirkland, WA, USA), and cultured in an endothelial cell medium (ScienCell, San Diego, CA, USA) according to the manufacturer's protocol. HA and HBVP were also purchased from ScienCell (San Diego, CA, USA), and cultured according to the manufacturer's recommended protocol. The cells were maintained in a humidified CO_2 incubator at 37 °C, and cultured in passage 8.

Human glioblastoma cell lines (T98G and U87MG) were purchased from the Korean Cell Line Bank (Seoul, Korea), and cultured in Dulbecco's modified Eagle medium (DMEM, Welgene, Daegu, Korea), which is supplemented with 10% (v/v) fetal bovine serum and 1% (v/v) penicillin-streptomycin in a humidified CO_2 incubator at 37 °C.

Collagen Preparation for 3D Cell Culture: Rat tail collagen type I (Corning, NY, USA) was purchased and diluted to a final concentration of 3 mg mL^{-1}, by adding 10× DMEM (Sigma-Aldrich, St. Louis, MO, USA), 1× DMEM (Welgene, Daegu, Korea), and 1 N sodium hydroxide (NaOH) (Sigma-Aldrich, St. Louis, MO, USA) according to the manufacturer's instructions. The entire procedure was performed on ice.

Construction of In Vitro Vasculature Within Cell-Embedded Collagen: Both HA and HBVP were embedded in sol state collagen by mixing them at a density of 2 × 10^5 cells mL^{-1}. The cell-mixed collagen, with a final concentration of 4 × 10^5 cells mL^{-1}, was injected into a 4 × 10 mm rectangular hydrogel chamber containing microneedles. The device was incubated at 37 °C for 30 min for collagen gelation to occur, and the microneedles were removed once the collagen were gelated. Then, hollow and cylindrical channel, with the same dimensions as the microneedle, were formed. A high-density suspension of HBMEC (1 × 10^6 cells mL^{-1}) was seeded on the luminal surface of the collagen channel after 1 h of incubating the device with the cell culture medium. Additionally, the medium was infused into the endothelial cell-cultured channel, and then, changed to the optimized medium for the culture to remove nonadherent endothelial cells.

Estimation of Cell Viability: A staining solution for the live/dead assay is prepared by mixing calcein-AM (C1430; ThermoFisher, Waltham, MA, USA), propidium iodide (PI; P4564; Sigma-Aldrich, St. Louis, MO, USA), and Hoechst 33 342 (H3570; Invitrogen, Carlsbad, CA, USA) in the serum-free medium, with concentrations of 1 µM for calcein-AM, 1 µg mL^{-1} for PI, and 10 µg mL^{-1} for Hoechst 33 342. On day 5, all of the cells cultured in the chips were incubated with staining solutions at 37 °C for 30 min, and then, washed with cell culture media before fluorescence imaging. The cell viability was quantified by counting the individual green (live) and red (dead) cells in the images acquired from multiple chips ($n = 3$) and calculating the ratio of the number of live cells (green) to the total number of cells.

Immunocytochemistry: The chips were fixed with 4% (v/v) paraformaldehyde for 30 min, and then, permeabilized with 0.3% (v/v) Triton X-100 (Sigma-Aldrich, St. Louis, MO, USA) and 3% (w/v) bovine serum albumin (BSA; Sigma-Aldrich, St. Louis, MO, USA) in PBS for 1 h. Then, they were incubated with primary antibodies diluted in the 3% (w/v) BSA solution overnight at 4 °C. Subsequently, the chips were washed with PBS, and incubated with secondary antibodies diluted in the 3% (w/v) BSA solution for 2 h at room temperature range of 18 to 24 °C. The 4′,6-diamidino-2-phenylindole solution was added for 30 min to stain the nuclei. Confocal z-stack images were acquired using a Zeiss LSM700 confocal laser scanning microscope (CLSM, Zeiss, Oberkochen, Germany). The primary and secondary antibodies used for immunocytochemistry are listed in Table S1, Supporting Information.

Measurement and Estimation of Vascular Permeability: Three types of fluorescent dyes, namely 376 Da fluorescein sodium salt (Sigma-Aldrich, St. Louis, MO, USA) along with 4 and 40 kDa FITC-dextran (Sigma-Aldrich, St. Louis, MO, USA), were diluted in PBS at 10 µM, and used to measure the vascular permeability of the engineered brain endothelium. The medium for each reservoir was aspirated, and the FITC-dextran solution was induced into the endothelium. The solution filled the channel, and diffused through the intercellular gap to the collagen scaffold. Molecular transport was monitored by capturing the sequential fluorescence using a Zeiss LSM700 CLSM (Zeiss, Oberkochen, Germany). The fluorescence images were acquired at 1 min intervals for 5 min, and then, analyzed using MATLAB (MathWorks, Massachusetts, USA). Vascular permeability was quantified using the mean fluorescence intensity on both sides of the channel and its variation at time intervals, as previously reported.[89]

Cytokine Array: The medium soup was collected from the chip reservoirs, to analyze the production of cytokines of BBB and GBM chips. The medium sample was purified and measured using a human L1000 microarray (e-Biogen Inc., Seoul, Korea), following the manufacturer's protocol.

Inflammation Assay: TNF-α, which is a key factor in inflammation-associated diseases, was used to induce inflammatory conditions and verify the protective effect of the BBB. The matured brain endothelium was incubated with the culture medium, with 50 ng mL^{-1} of TNF-α (R&D Systems, Minneapolis, USA), for 2 or 24 h. Subsequently, permeability was quantified as previously summarized.

Temporary Opening of the BBB with Mannitol and Gintonin: Both gintonin and D-mannitol (Sigma-Aldrich, St. Louis, MO, USA) were used for investigating the transient opening of the BBB. Gintonin, devoid of ginseng saponins, was prepared from Panax ginseng based on a previous study,[90] and dissolved in 0.9% saline. The gintonin and D-mannitol solutions were diluted in the medium, and introduced to the endothelium through gravity-driven flow until the medium height of the reservoirs was balanced. The BBB-opening agent-treated brain endothelium was incubated at 37 °C for 15, 30, or 60 min. The solution was then washed with fresh medium. Additional incubation for 24 h was performed to induce the recovery of the loosened barrier function. Moreover, vascular permeability was measured to verify the opening and recovery of the BBB similar to what is described above.

Morphological Analysis of Tumor Cells: The morphological changes of brain tumor cells were quantitatively determined by the aspect ratio and cell shape index (CSI) representing the elongation and circularity of the

cells. Elongated cells exhibit a high aspect ratio and a CSI value close to 0. Both values were calculated as depicted below[91]

$$\text{Aspect ratio} = \text{length} / \text{width} \quad (1)$$

$$\text{CSI} = 4\pi \times \text{area} / (\text{perimeter})^2 \quad (2)$$

Testing of Chemotherapeutic Agents: TMZ (Sigma-Aldrich, St. Louis, MO, USA) and VCR (Sigma-Aldrich, St. Louis, MO, USA) were dissolved in DMSO at 10 and 5 mg mL^{-1}, respectively, to prepare the stock solution. Additionally, DOX (Sigma-Aldrich, St. Louis, MO, USA) was dissolved in water at a concentration of 10 mg mL^{-1}. TMZ, VCR, and DOX were diluted to complete the cell culture medium, and infused into the brain endothelium for 4 days.

RNA Sequencing Experiment of GBM: GBM spheroids were harvested from the GBM chips, and used for analyzing the gene expression via RNA sequencing. First, the channel embedded with the GBM spheroids was exposed to 1% (w/v) Pluronic F127 solution (Sigma-Aldrich, St. Louis, MO, USA), to facilitate the isolation. Then, the GBM spheroid-embedded collagen was pushed by repeated pipetting in the microchannels. This process is illustrated in Figure S8A, Supporting Information. The isolated GBM spheroids were dissolved in TRIzol reagent (Sigma-Aldrich, St. Louis, MO, USA). Following the service provider's protocol, the samples were purified and used for the RNA sequencing experiments (e-Biogen Inc., Seoul, Korea).

Statistical Analysis: All quantitative data are presented as mean ± standard error of the mean values. Statistical analyses were performed using unpaired *t*-tests in Prism (GraphPad, San Diego, CA, USA). The *p*-values <0.05, 0.01, 0.005, and 0.001, which were considered significant, were used for determining the statistical significance.

Supporting Information

Supporting Information is available from the Wiley Online Library or from the author.

Acknowledgements

This study was supported by National Research Foundation of Korea (NRF) funded by the Korean Government (MSIT) (2021R1A2B5B02096828), Brain Research Program of the National Research Foundation of Korea (NRF) funded by the Ministry of Science and ICT (2018M3C7A1056896), Bio & Medical Technology Development Program of the National Research Foundation (NRF) funded by the Korean government (MSIT) (No. 2020M3E5D907974412 and 2017M3A7B4049850), and KIST Institutional Program (2E30965 and 2E30966).

Conflict of Interest

The authors declare no conflict of interest.

Author Contributions

S.S, S.Y.N, K.L, N.C, and H.N.K. designed the experiments. S.S. fabricated the devices, performed experiments, analyzed and visualized data, and wrote the manuscript. S.Y.N. supplied the materials for experiments. N.C. provided MATLAB code for analyzing data. K.L., N.C., and H.N.K. acquired fund and supervised the project and reviewed and revised the manuscript.

Data Availability Statement

The data that support the findings of this study are available from the corresponding author upon reasonable request.

Keywords

blood–brain barrier, blood–brain barrier-opening, drug delivery, in vitro model, tumor microenvironment

Received: July 15, 2021
Revised: September 20, 2021
Published online: November 5, 2021

[1] J. Pitt, A. Marabelle, A. Eggermont, J.-C. Soria, G. Kroemer, L. Zitvogel, *Ann. Oncol.* **2016**, *27*, 1482.
[2] V. Gouirand, F. Guillaumond, S. Vasseur, *Front. Oncol.* **2018**, *8*, 117.
[3] Y. Kim, M. A. Stolarska, H. G. Othmer, *Prog. Biophys. Mol. Biol.* **2011**, *106*, 353.
[4] Y. Yuan, Y.-C. Jiang, C.-K. Sun, Q.-M. Chen, *Oncol. Rep.* **2016**, *35*, 2499.
[5] H. Patel, P. Nilendu, D. Jahagirdar, J. K. Pal, N. K. Sharma, *Cancer Biol. Therapy* **2018**, *19*, 3.
[6] A. Cretu, P. C. Brooks, *J. Cell. Physiol.* **2007**, *213*, 391.
[7] M. E. Bregenzer, E. N. Horst, P. Mehta, C. M. Novak, S. Raghavan, C. S. Snyder, G. Mehta, *PLoS One* **2019**, *14*, e0216564.
[8] N. Chaicharoenaudomrung, P. Kunhorm, P. Noisa, *World J. Stem Cells* **2019**, *11*, 1065.
[9] H. N. Kim, N. L. Habbit, C. Y. Su, N. Choi, E. H. Ahn, E. A. Lipke, D. H. Kim, *Adv. Funct. Mater.* **2019**, *29*, 1807553.
[10] M. Devarasetty, S. D. Forsythe, E. Shelkey, S. Soker, *Tissue Eng. Regener. Med.* **2020**, *17*, 759.
[11] Y. Nashimoto, R. Okada, S. Hanada, Y. Arima, K. Nishiyama, T. Miura, R. Yokokawa, *Biomaterials* **2020**, *229*, 119547.
[12] K. Haase, G. S. Offeddu, M. R. Gillrie, R. D. Kamm, *Adv. Funct. Mater.* **2020**, *30*, 2002444.
[13] D. Truong, R. Fiorelli, E. S. Barrientos, E. L. Melendez, N. Sanai, S. Mehta, M. Nikkhah, *Biomaterials* **2019**, *198*, 63.
[14] A. Sobrino, D. T. Phan, R. Datta, X. Wang, S. J. Hachey, M. Romero-López, E. Gratton, A. P. Lee, S. C. George, C. C. Hughes, *Sci. Rep.* **2016**, *6*, 31589.
[15] A. S. Nunes, A. S. Barros, E. C. Costa, A. F. Moreira, I. J. Correia, *Biotechnol. Bioeng.* **2019**, *116*, 206.
[16] S. Seo, H. Kim, J. H. Sung, N. Choi, K. Lee, H. N. Kim, *Biomaterials* **2020**, *232*, 119732.
[17] M. L. Moya, S. C. George, *Curr. Opin. Chem. Eng.* **2014**, *3*, 102.
[18] V. Roy, B. Magne, M. Vaillancourt-Audet, M. Blais, S. Chabaud, E. Grammond, L. Piquet, J. Fradette, I. Laverdière, V. J. Moulin, *Biomed Res. Int.* **2020**, *2020*, 6051210.
[19] P. Moshayedi, G. Ng, J. C. Kwok, G. S. Yeo, C. E. Bryant, J. W. Fawcett, K. Franze, J. Guck, *Biomaterials* **2014**, *35*, 3919.
[20] C. L. Wilson, S. L. Hayward, S. Kidambi, *RSC Adv.* **2016**, *6*, 34447.
[21] E. B. Brown, R. B. Campbell, Y. Tsuzuki, L. Xu, P. Carmeliet, D. Fukumura, R. K. Jain, *Nat. Med.* **2001**, *7*, 864.
[22] C. C. Reyes-Aldasoro, I. Wilson, V. E. Prise, P. R. Barber, M. Ameer-Beg, B. Vojnovic, V. J. Cunningham, G. M. Tozer, *Microcirculation* **2008**, *15*, 65.
[23] W. Yuan, Y. Lv, M. Zeng, B. M. Fu, *Microvasc. Res.* **2009**, *77*, 166.
[24] M. Bisht, D. Dhasmana, S. Bist, *Ind. J. Pharmacol.* **2010**, *42*, 2.
[25] J. Kim, K.-T. Lee, J. S. Lee, J. Shin, B. Cui, K. Yang, Y. S. Choi, N. Choi, S. H. Lee, J.-H. Lee, Y.-S. Bahn, S.-W. Cho, *Nat. Biomed. Eng.* **2021**, *5*, 830.
[26] N. J. Abbott, A. A. Patabendige, D. E. Dolman, S. R. Yusof, D. J. Begley, *Neurobiol. Dis.* **2010**, *37*, 13.
[27] D. Bonkowski, V. Katyshev, R. D. Balabanov, A. Borisov, P. Dore-Duffy, *Fluids Barriers CNS* **2011**, *8*, 8.
[28] M. V. Sofroniew, *Nat. Rev. Neurosci.* **2015**, *16*, 249.
[29] D. B. Vieira, L. F. Gamarra, *Int. J. Nanomed.* **2016**, *11*, 5381.

[30] J. J. Mulvihill, E. M. Cunnane, A. M. Ross, J. T. Duskey, G. Tosi, A. M. Grabrucker, *Nanomedicine* **2020**, *15*, 205.
[31] E. E. Konofagou, Y.-S. Tunga, J. Choia, T. Deffieuxa, B. Baseria, F. Vlachosa, *Curr. Pharm. Biotechnol.* **2012**, *13*, 1332.
[32] S. I. Rapoport, *Cell. Mol. Neurobiol.* **2000**, *20*, 217.
[33] D.-G. Kim, M. Jang, S.-H. Choi, H.-J. Kim, H. Jhun, H.-C. Kim, H. Rhim, I.-H. Cho, S.-Y. Nah, *Int. J. Biol. Macromol.* **2018**, *114*, 1325.
[34] H.-L. Liu, Y.-Y. Wai, W.-S. Chen, J.-C. Chen, P.-H. Hsu, X.-Y. Wu, W.-C. Huang, T.-C. Yen, J.-J. Wang, *Ultrasound Med. Biol.* **2008**, *34*, 598.
[35] K.-T. Chen, K.-C. Wei, H.-L. Liu, *Front. Pharmacol.* **2019**, *10*, 86.
[36] K. Hynynen, N. McDannold, N. A. Sheikov, F. A. Jolesz, N. Vykhodtseva, *Neuroimage* **2005**, *24*, 12.
[37] C.-H. Fan, H.-L. Liu, C.-Y. Ting, Y.-H. Lee, C.-Y. Huang, Y.-J. Ma, K.-C. Wei, T.-C. Yen, C.-K. Yeh, *PLoS One* **2014**, *9*, e96327.
[38] O. Trédan, C. M. Galmarini, K. Patel, I. F. Tannock, *J. Natl. Cancer Inst.* **2007**, *99*, 1441.
[39] S. Y. Lee, *Genes Dis.* **2016**, *3*, 198.
[40] A. Ramão, M. Gimenez, H. J. Laure, C. Izumi, R. C. dos Santos Vida, S. Oba-Shinjo, S. K. N. Marie, J. C. Rosa, *Proteome Sci.* **2012**, *10*, 53.
[41] R. H. Farnsworth, M. Lackmann, M. G. Achen, S. A. Stacker, *Oncogene* **2014**, *33*, 3496.
[42] M. K. Gupta, R.-Y. Qin, *World J Gastroenterol.* **2003**, *9*, 1144.
[43] S. Gately, W. W. Li, *Semin. Oncol.* **2004**, *31*, 2.
[44] H. Kidoya, N. Kunii, H. Naito, F. Muramatsu, Y. Okamoto, T. Nakayama, N. Takakura, *Oncogene* **2012**, *31*, 3254.
[45] E. M. Langenfeld, J. Langenfeld, *Mol. Cancer Res.* **2004**, *2*, 141.
[46] P. P. Ongusaha, J. C. Kwak, A. J. Zwible, S. Macip, S. Higashiyama, N. Taniguchi, L. Fang, S. W. Lee, *Cancer Res.* **2004**, *64*, 5283.
[47] E. Franzè, C. Stolfi, E. Troncone, P. Scarozza, G. Monteleone, *Cancers* **2020**, *12*, 252.
[48] J. Ishida, T. Hashimoto, Y. Hashimoto, S. Nishiwaki, T. Iguchi, S. Harada, T. Sugaya, H. Matsuzaki, R. Yamamoto, N. Shiota, *J. Biol. Chem.* **2004**, *279*, 26274.
[49] H. Kidoya, M. Ueno, Y. Yamada, N. Mochizuki, M. Nakata, T. Yano, R. Fujii, N. Takakura, *EMBO J.* **2008**, *27*, 522.
[50] K. Tatemoto, K. Takayama, M.-X. Zou, I. Kumaki, W. Zhang, K. Kumano, M. Fujimiya, *Regul. Pept.* **2001**, *99*, 87.
[51] Y. Yeung, K. McDonald, T. Grewal, L. Munoz, *Br. J. Pharmacol.* **2013**, *168*, 591.
[52] S. Setrerrahmane, H. Xu, *Mol. Cancer* **2017**, *16*, 153.
[53] X. Cao, R. Ashfaq, F. Cheng, S. Maharjan, J. Li, G. Ying, S. Hassan, H. Xiao, K. Yue, Y. S. Zhang, *Adv. Funct. Mater.* **2019**, *29*, 1807173.
[54] D. Wang, C. Wang, L. Wang, Y. Chen, *Drug Delivery* **2019**, *26*, 551.
[55] K. E. Warren, *Front. Oncol.* **2018**, *8*, 239.
[56] I. Sardi, G. la Marca, S. Cardellicchio, L. Giunti, S. Malvagia, L. Genitori, M. Massimino, M. de Martino, M. G. Giovannini, *Am. J. Cancer Res.* **2013**, *3*, 424.
[57] Y. Lee, J.-K. Lee, S. H. Ahn, J. Lee, D.-H. Nam, *Lab. Invest.* **2016**, *96*, 137.
[58] M. McCord, Y.-s. Mukouyama, M. R. Gilbert, S. Jackson, *Front. Cell. Neurosci.* **2017**, *11*, 318.
[59] Z. Zhong, D. M. Virshup, *Mol. Pharmacol.* **2020**, *97*, 72.
[60] M. Kamino, M. Kishida, T. Kibe, K. Ikoma, M. Iijima, H. Hirano, M. Tokudome, L. Chen, C. Koriyama, K. Yamada, *Cancer Sci.* **2011**, *102*, 540.
[61] R. R. Varma, S. M. Hector, K. Clark, W. R. Greco, L. Hawthorn, L. Pendyala, *Oncol. Rep.* **2005**, *14*, 925.
[62] K. Willert, R. Nusse, *Curr. Opin. Genet. Dev.* **1998**, *8*, 95.
[63] B. Saha, T. Mathur, J. J. Tronolone, M. Chokshi, G. K. Lokhande, A. Selahi, A. K. Gaharwar, V. Afshar-Kharghan, A. K. Sood, G. Bao, *Sci. Adv.* **2021**, *7*, eabg5283.
[64] J. S. Jeon, S. Bersini, M. Gilardi, G. Dubini, J. L. Charest, M. Moretti, R. D. Kamm, *Proc. Natl. Acad. Sci. USA* **2015**, *112*, 214.
[65] Y. Choi, E. Hyun, J. Seo, C. Blundell, H. C. Kim, E. Lee, S. H. Lee, A. Moon, W. K. Moon, D. Huh, *Lab Chip* **2015**, *15*, 3350.
[66] B. A. Hassell, G. Goyal, E. Lee, A. Sontheimer-Phelps, O. Levy, C. S. Chen, D. E. Ingber, *Cell Rep.* **2017**, *21*, 508.
[67] J. M. Ayuso, S. Rehman, M. Virumbrales-Munoz, P. H. McMinn, P. Geiger, C. Fitzgerald, T. Heaster, M. C. Skala, D. J. Beebe, *Sci. Adv.* **2021**, *7*, eabc2331.
[68] A. Marino, O. Tricinci, M. Battaglini, C. Filippeschi, V. Mattoli, E. Sinibaldi, G. Ciofani, *Small* **2018**, *14*, 1702959.
[69] B. S. Kim, W. W. Cho, G. Gao, M. Ahn, J. Kim, D. W. Cho, *Small Methods* **2021**, *5*, 2100072.
[70] Y. I. Wang, H. E. Abaci, M. L. Shuler, *Biotechnol. Bioeng.* **2017**, *114*, 184.
[71] S. I. Ahn, Y. J. Sei, H.-J. Park, J. Kim, Y. Ryu, J. J. Choi, H.-J. Sung, T. J. MacDonald, A. I. Levey, Y. Kim, *Nat. Commun.* **2020**, *11*, 175.
[72] G. D. Vatine, R. Barrile, M. J. Workman, S. Sances, B. K. Barriga, M. Rahnama, S. Barthakur, M. Kasendra, C. Lucchesi, J. Kerns, *Cell Stem Cell* **2019**, *24*, 995.
[73] M. Campisi, Y. Shin, T. Osaki, C. Hajal, V. Chiono, R. D. Kamm, *Biomaterials* **2018**, *180*, 117.
[74] B. M. Maoz, A. Herland, E. A. FitzGerald, T. Grevesse, C. Vidoudez, A. R. Pacheco, S. P. Sheehy, T.-E. Park, S. Dauth, R. Mannix, *Nat. Biotechnol.* **2018**, *36*, 865.
[75] T.-E. Park, N. Mustafaoglu, A. Herland, R. Hasselkus, R. Mannix, E. A. FitzGerald, R. Prantil-Baun, A. Watters, O. Henry, M. Benz, H. Sanchez, H. J. McCrea, L. C. Goumnerova, H. W. Song, S. P. Palecek, E. Shusta, D. E. Ingber, *Nat. Commun.* **2019**, *10*, 2621.
[76] S. Bang, S.-R. Lee, J. Ko, K. Son, D. Tahk, J. Ahn, C. Im, N. L. Jeon, *Sci. Rep.* **2017**, *7*, 8083.
[77] Y. Shin, S. H. Choi, E. Kim, E. Bylykbashi, J. A. Kim, S. Chung, D. Y. Kim, R. D. Kamm, R. E. Tanzi, *Adv. Sci.* **2019**, *6*, 1900962.
[78] X. Zhao, R. Chen, M. Liu, J. Feng, J. Chen, K. Hu, *Acta Pharm. Sin. B* **2017**, *7*, 541.
[79] W. Sin, Q. Aftab, J. Bechberger, J. Leung, H. Chen, C. Naus, *Oncogene* **2016**, *35*, 1504.
[80] P. Lu, Y. Wang, X. Liu, H. Wang, X. Zhang, K. Wang, Q. Wang, R. Hu, *Med. Oncol.* **2016**, *33*, 66.
[81] I. F. Sena, A. E. Paiva, P. H. Prazeres, P. O. Azevedo, L. Lousado, S. K. Bhutia, A. B. Salmina, A. Mintz, A. Birbrair, *Cancer Med.* **2018**, *7*, 1232.
[82] M. G. McCoy, D. Nyanyo, C. K. Hung, J. P. Goerger, W. R. Zipfel, R. M. Williams, N. Nishimura, C. Fischbach, *Sci. Rep.* **2019**, *9*, 9069.
[83] H.-Y. Jung, L. Fattet, J. Yang, *Clin. Cancer Res.* **2015**, *21*, 962.
[84] A. H. Schinkel, *Adv. Drug Delivery Rev.* **1999**, *36*, 179.
[85] W. M. Pardridge, *NeuroRx* **2005**, *2*, 3.
[86] T. Hartung, *Parkinsonism Relat. Disord.* **2008**, *14*, S81.
[87] S. Seo, C.-H. Choi, K. S. Yi, S. U. Kim, K. Lee, N. Choi, H. J. Lee, S.-H. Cha, H. N. Kim, *Biofabrication* **2021**, *13*, 035039.
[88] S. H. Kim, S.-K. Im, S.-J. Oh, S. Jeong, E.-S. Yoon, C. J. Lee, N. Choi, E.-M. Hur, *Nat. Commun.* **2017**, *8*, 14346.
[89] J. A. Kim, H. N. Kim, S.-K. Im, S. Chung, J. Y. Kang, N. Choi, *Biomicrofluidics* **2015**, *9*, 024115.
[90] M.-K. Pyo, S.-H. Choi, S.-H. Hwang, T.-J. Shin, B.-H. Lee, S.-M. Lee, Y.-H. Lim, D.-H. Kim, S.-Y. Nah, *J. Ginseng Res.* **2011**, *35*, 92.
[91] T. Abdulla, L. Luna-Zurita, J. L. De La Pompa, J.-M. Schleich, R. Summers, *Comput. Methods Programs Biomed.* **2013**, *111*, 435.